

# Comparison of two x-ray phase-contrast imaging methods with a microfocus source

T. Zhou,<sup>1,\*</sup> U. Lundström,<sup>1</sup> T. Thüring,<sup>2,3</sup> S. Rutishauser,<sup>2,3</sup> D. H. Larsson,<sup>1</sup> M. Stampanoni,<sup>2,3</sup> C. David,<sup>2</sup> H. M. Hertz,<sup>1</sup> and A. Burvall<sup>1</sup>

<sup>1</sup>Biomedical and X-ray Physics, KTH Royal Institute of Technology, Albanova, SE-10691, Stockholm, Sweden

<sup>2</sup>Paul Scherrer Institute, Villigen PSI, Switzerland

<sup>3</sup>Institute for Biomedical Engineering, Swiss Federal Institute of Technology, Zurich, Switzerland  
[tunhe.zhou@biox.kth.se](mailto:tunhe.zhou@biox.kth.se)

**Abstract:** We present a comparison for high-resolution imaging with a laboratory source between grating-based (GBI) and propagation-based (PBI) x-ray phase-contrast imaging. The comparison is done through simulations and experiments using a liquid-metal-jet x-ray microfocus source. Radiation doses required for detection in projection images are simulated as a function of the diameter of a cylindrical sample. Using monochromatic radiation, simulations show a lower dose requirement for PBI for small object features and a lower dose for GBI for larger object features. Using polychromatic radiation, such as that from a laboratory microfocus source, experiments and simulations show a lower dose requirement for PBI for a large range of feature sizes. Tested on a biological sample, GBI shows higher noise levels than PBI, but its advantage of quantitative refractive index reconstruction for multi-material samples becomes apparent.

©2013 Optical Society of America

**OCIS codes:** (110.7440) X-ray imaging; (110.2960) Image analysis; (110.6760) Talbot and self-imaging effects.

---

## References and links

1. R. Raupach and T. Flohr, "Performance evaluation of x-ray differential phase contrast computed tomography (PCT) with respect to medical imaging," *Med. Phys.* **39**(8), 4761–4774 (2012).
2. U. Lundström, D. H. Larsson, A. Burvall, P. A. Takman, L. Scott, H. Brismar, and H. M. Hertz, "X-ray phase contrast for CO<sub>2</sub> microangiography," *Phys. Med. Biol.* **57**(9), 2603–2617 (2012).
3. O. Hemberg, M. Otendal, and H. M. Hertz, "Liquid-metal-jet anode electron-impact x-ray source," *Appl. Phys. Lett.* **83**(7), 1483–1485 (2003).
4. D. H. Larsson, P. A. C. Takman, U. Lundström, A. Burvall, and H. M. Hertz, "A 24 keV liquid-metal-jet x-ray source for biomedical applications," *Rev. Sci. Instrum.* **82**(12), 123701 (2011).
5. S. W. Wilkins, T. E. Gureyev, D. Gao, A. Pogany, and A. W. Stevenson, "Phase-contrast imaging using polychromatic hard X-rays," *Nature* **384**(6607), 335–338 (1996).
6. T. Weitkamp, A. Diaz, C. David, F. Pfeiffer, M. Stampanoni, P. Cloetens, and E. Ziegler, "X-ray phase imaging with a grating interferometer," *Opt. Express* **13**(16), 6296–6304 (2005).
7. F. Pfeiffer, T. Weitkamp, O. Bunk, and C. David, "Phase retrieval and differential phase-contrast imaging with low-brilliance X-ray sources," *Nat. Phys.* **2**(4), 258–261 (2006).
8. C. Parham, Z. Zhong, D. M. Connor, L. D. Chapman, and E. D. Pisano, "Design and implementation of a compact low-dose diffraction enhanced medical imaging system," *Acad. Radiol.* **16**(8), 911–917 (2009).
9. I. Nesch, D. P. Fogarty, T. Tzvetkov, B. Reinhard, A. C. Walus, G. Khelashvili, C. Muehleman, and D. Chapman, "The design and application of an in-laboratory diffraction-enhanced x-ray imaging instrument," *Rev. Sci. Instrum.* **80**(9), 093702 (2009).
10. T. Thüring, T. Zhou, U. Lundström, A. Burvall, S. Rutishauser, C. David, H. M. Hertz, and M. Stampanoni, "X-ray grating interferometry with a liquid-metal-jet source," *Appl. Phys. Lett.* **103**(9), 091105 (2013).
11. D. H. Larsson, U. Lundström, U. K. Westermark, M. Arsenian Henriksson, A. Burvall, and H. M. Hertz, "First application of liquid-metal-jet sources for small-animal imaging: high-resolution CT and phase-contrast tumor demarcation," *Med. Phys.* **40**(2), 021909 (2013).
12. D. Hahn, P. Thibault, M. Bech, M. Stockmar, S. Schleede, I. Zanette, A. Rack, T. Weitkamp, A. Sztrókey, T. Schlossbauer, F. Bamberg, M. Reiser, and F. Pfeiffer, "Numerical comparison of X-ray differential phase contrast and attenuation contrast," *Biomed. Opt. Express* **3**(6), 1141–1148 (2012).

13. P. Modregger, B. R. Pinzer, T. Thüring, S. Rutishauser, C. David, and M. Stampanoni, "Sensitivity of X-ray grating interferometry," *Opt. Express* **19**(19), 18324–18338 (2011).
14. T. Köhler, K. Jürgen Engel, and E. Roessl, "Noise properties of grating-based x-ray phase contrast computed tomography," *Med. Phys.* **38**(S1), S106–S116 (2011).
15. R. Raupach and T. G. Flohr, "Analytical evaluation of the signal and noise propagation in x-ray differential phase-contrast computed tomography," *Phys. Med. Biol.* **56**(7), 2219–2244 (2011).
16. E. Fredenberg, M. Danielsson, J. W. Stayman, J. H. Siewerdsen, and M. Aslund, "Ideal-observer detectability in photon-counting differential phase-contrast imaging using a linear-systems approach," *Med. Phys.* **39**(9), 5317–5335 (2012).
17. P. C. Diemoz, A. Bravin, and P. Coan, "Theoretical comparison of three X-ray phase-contrast imaging techniques: propagation-based imaging, analyzer-based imaging and grating interferometry," *Opt. Express* **20**(3), 2789–2805 (2012).
18. E. Pagot, S. Fiedler, P. Cloetens, A. Bravin, P. Coan, K. Fezzaa, J. Baruchel, J. Härtwig, K. von Smitten, M. Leidenius, M. L. Karjalainen-Lindsberg, and J. Keyriläinen, "Quantitative comparison between two phase contrast techniques: diffraction enhanced imaging and phase propagation imaging," *Phys. Med. Biol.* **50**(4), 709–724 (2005).
19. P. C. Diemoz, A. Bravin, M. Langer, and P. Coan, "Analytical and experimental determination of signal-to-noise ratio and figure of merit in three phase-contrast imaging techniques," *Opt. Express* **20**(25), 27670–27690 (2012).
20. V. Revol, C. Kottler, R. Kaufmann, U. Straumann, and C. Urban, "Noise analysis of grating-based x-ray differential phase contrast imaging," *Rev. Sci. Instrum.* **81**(7), 073709 (2010).
21. G. H. Chen, J. Zambelli, K. Li, N. Bevins, and Z. H. Qi, "Scaling law for noise variance and spatial resolution in differential phase contrast computed tomography," *Med. Phys.* **38**(2), 584–588 (2011).
22. K. Li, N. Bevins, J. Zambelli, and G. H. Chen, "Fundamental relationship between the noise properties of grating-based differential phase contrast CT and absorption CT: theoretical framework using a cascaded system model and experimental validation," *Med. Phys.* **40**(2), 021908 (2013).
23. J. Zambelli, N. Bevins, Z. Qi, and G. H. Chen, "Radiation dose efficiency comparison between differential phase contrast CT and conventional absorption CT," *Med. Phys.* **37**(6), 2473–2479 (2010).
24. X. Tang, Y. Yang, and S. Tang, "Characterization of imaging performance in differential phase contrast CT compared with the conventional CT--noise power spectrum NPS(k)," *Med. Phys.* **38**(7), 4386–4395 (2011).
25. T. Weber, P. Bartl, F. Bayer, J. Durst, W. Haas, T. Michel, A. Ritter, and G. Anton, "Noise in x-ray grating-based phase-contrast imaging," *Med. Phys.* **38**(7), 4133–4140 (2011).
26. T. Zhou, U. Lundström, D. H. Larsson, H. M. Hertz, and A. Burvall, "Low-dose phase-contrast X-ray imaging: a comparison of two methods," *J. Phys. Conf. Ser.* **463**, 012041 (2013).
27. F. Pfeiffer, M. Bech, O. Bunk, P. Kraft, E. F. Eikenberry, Ch. Brönnimann, C. Grünzweig, and C. David, "Hard-X-ray dark-field imaging using a grating interferometer," *Nat. Mater.* **7**(2), 134–137 (2008).
28. A. Burvall, U. Lundström, P. A. C. Takman, D. H. Larsson, and H. M. Hertz, "Phase retrieval in X-ray phase-contrast imaging suitable for tomography," *Opt. Express* **19**(11), 10359–10376 (2011).
29. F. Pfeiffer, C. Kottler, O. Bunk, and C. David, "Hard x-ray phase tomography with low-brilliance sources," *Phys. Rev. Lett.* **98**(10), 108105 (2007).
30. G. W. Faris and R. L. Byer, "Three-dimensional beam-deflection optical tomography of a supersonic jet," *Appl. Opt.* **27**(24), 5202–5212 (1988).
31. D. Paganin, S. C. Mayo, T. E. Gureyev, P. R. Miller, and S. W. Wilkins, "Simultaneous phase and amplitude extraction from a single defocused image of a homogeneous object," *J. Microsc.* **206**(1), 33–40 (2002).
32. J. Vlassenbroeck, M. Dierick, B. Masschaele, V. Cnudde, L. van Hoorebeke, and P. Jacobs, "Software tools for quantification of X-ray microtomography," *Nucl. Instrum. Methods Phys. Res. A* **580**(1), 442–445 (2007).
33. D. M. Paganin, *Coherent X-Ray Optics* (Oxford University, 2009).
34. J. H. Hubbell and S. M. Seltzer, *Tables of X-Ray Mass Attenuation Coefficients and Mass Energy-Absorption Coefficients from 1 keV to 20 MeV for Elements Z = 1 to 92 and 48 Additional Substances of Dosimetric Interest* (Radiation and Biomolecular Physics Division, PML, NIST, 1996).
35. L. Kissel, "RTAB: the Rayleigh scattering database," *Radiat. Phys. Chem.* **59**(2), 185–200 (2000).
36. J. Baró, J. Sempau, J. M. Fernandezvarea, and F. Salvat, "Penelope - an algorithm for Monte-Carlo simulation of the penetration and energy-loss of electrons and positrons in matter," *Nucl. Instrum. Methods Phys. Res. B* **100**(1), 31–46 (1995).
37. H. H. Barrett and K. J. Myers, *Foundations of Image Science* (John Wiley, 2003).
38. U. Lundström, D. H. Larsson, A. Burvall, L. Scott, U. K. Westermark, M. Wilhelm, M. Arsenian Henriksson, and H. M. Hertz, "X-ray phase-contrast CO<sub>2</sub> angiography for sub-10 μm vessel imaging," *Phys. Med. Biol.* **57**(22), 7431–7441 (2012).
39. A. Rose, "The sensitivity performance of the human eye on an absolute scale," *J. Opt. Soc. Am.* **38**(2), 196–208 (1948).
40. A. Fandos-Morera, M. Prats-Esteve, J. M. Tura-Soteras, and A. Traveria-Cros, "Breast tumors: composition of microcalcifications," *Radiology* **169**(2), 325–327 (1988).

## 1. Introduction

For x-ray phase-contrast methods to become practical for small-animal or medical imaging, laboratory sources are needed. As phase-contrast imaging allows for a lower dose than absorption imaging for high resolution [1, 2], this is where the medical impact of the methods is likely to be. High-resolution medical or small-animal imaging requires x-ray sources with small emitting areas that still give sufficient flux for reasonable exposure times, and liquid-metal-jet sources have the potential for this [3, 4]. Using a liquid-metal-jet microfocus source, we directly compare two phase-contrast methods relevant for laboratory imaging with respect to the dose required for detection of features of different sizes.

Two phase-contrast methods that function relatively well with polychromatic x-rays are propagation-based (or in-line) phase-contrast imaging (PBI) [5], and grating-based (or Talbot) phase-contrast imaging (GBI) [6]. PBI requires high spatial coherence, and hence a small source. GBI can be used with an extended source, such as a conventional x-ray tube, if an additional grating is placed at the source [7]. An extended source with higher power has the advantage of shortening the exposure time, but the image resolution will be correspondingly lower. For high-resolution imaging, a source with small emitting surface is required. Analyzer-based imaging (ABI) can also be applied with polychromatic laboratory sources by using monochromators [8, 9].

The use of liquid-metal-jet sources for grating-based imaging was recently demonstrated [10]. This technology uses regenerate jet of liquid metal as anode which relaxes the limitation at high e-beam power density. These sources are currently being operated at an e-beam power density of 600-1300 kW/mm<sup>2</sup> (7-20 μm spot size) [4, 11] and there is potential for significant increase, making them an interesting option for phase-contrast imaging.

X-ray phase-contrast imaging is normally limited by noise, so to compare the two phase-contrast methods, noise characteristics must be considered. Using or assuming synchrotron radiation, the noise characteristics of the phase signal for GBI have been investigated by experiments [12, 13] and simulations [13–16]. Comparisons of the signal-to-noise ratio (SNR) of different phase-contrast methods have been performed both theoretically and experimentally [17–19]. Using conventional x-ray tubes, the noise characteristics of the phase signal have been investigated experimentally [20–24]. Using a microfocus source, the covariance matrix of the three image quantities has been studied [25]. In many cases, comparisons to absorption imaging have been made – some to conventional absorption imaging, some to the absorption signal obtained from GBI.

Taking the size of the object details into account, the dependence of noise on spatial resolution for GBI has been established and compared to absorption imaging [21], finding that grating-based phase contrast has lower noise than absorption imaging for fine details. A relation between dose and spatial resolution has been established numerically for grating-based tomography [1] and for propagation-based imaging [2], though under such different circumstances that it is difficult to compare them directly. Both show that phase-contrast imaging requires lower dose than absorption imaging for fine object features. As GBI and PBI are the most widely used methods for laboratory-based phase-contrast imaging, we extend the comparisons by comparing the two methods directly to each other under similar conditions. The comparison is done, using simulations and experiments, mainly for 2D projections, and some experimental 3D tomographic data are also presented. We use a liquid-metal-jet x-ray source, deeming this a promising technique for future high-resolution applications in small-animal and medical imaging.

This comparison is done under as similar conditions as possible, but due to the inherent differences between the two methods there will be differences in the conditions. In particular, optimal source-to-object and source-to-detector distances are not the same for the two methods. If the distances were chosen according to the propagation-based method, they would not fit the requirements for a Talbot interferometer with available gratings. If the distances

were instead optimized for the Talbot interferometer, the object-to-detector distance would be so short that very little phase contrast would be generated using the propagation-based method. Having established that the distances must be different, they can still be chosen with care. One option is to use the same total source-to-detector distance, as this gives the same length of the arrangement and hence the same photon counts at the detector, absorption in gratings excluded. Another option, which was used here, is using the same source-to-object distance, as this gives the same doses for equal exposure times. The distances of the grating-based method were chosen to fulfill the requirements of a Talbot interferometer. Keeping the source-to-object distance the same, the object-to-detector distance of the propagation-based method was limited by the detector size. It was chosen to keep the region of interest (ROI) of the largest object we used smaller than the field of view of the detector.

The two methods also differ in detector requirements. GBI is usually used with large pixels which allow the use of more efficient detectors. PBI requires high-resolution detectors to resolve the characteristic edge enhancements. As comparison conditions should be as similar as possible, we have used the same high-resolution detector for both methods, even though the effective detector element is smaller than that normally used for grating-based imaging.

Another issue relevant to the comparison is the use of a liquid bath. For grating-based imaging, objects are often immersed in a liquid bath to avoid phase-wrapping at the edges. This is a drawback from a noise point of view, as the bath absorbs radiation that has passed through the object and in special cases, such as for the phantom considered in this paper, it also lowers the contrast. Propagation-based imaging requires no liquid bath, but in this comparison the bath was used for both methods to make conditions as similar as possible.

Finally, the two methods provide different images. GBI generates phase, amplitude, and dark-field images, while single-distance PBI provides only the phase. In special cases, such as for a homogeneous sample, absorption information can be obtained from the phase distribution but does not add any new information. This comparison uses the phase images only. For simple objects with low absorption, like the phantom used in the present study, the phase image will dominate and most of the object information is in the phase image [26].

## 2. Methods

### 2.1 Experimental arrangements and samples

The experiments were performed using a liquid-metal-jet x-ray source from Excillum with a Ga/In/Sn alloy. An electron beam of 0.8 mA current and 50 kV acceleration voltage was focused onto the metal jet at 5° angle between the surface normal and the electron beam, as shown in Fig. 1. This yields an elliptical spot, almost Gaussian in shape, with a full width at half maximum (FWHM) of  $\sim 3.6 \mu\text{m} \times 6.8 \mu\text{m}$ . Compared to the spot size of  $\sim 7 \mu\text{m} \times 7 \mu\text{m}$  normally achieved with 45° incident angle [11], the smaller spot size in the direction perpendicular to the grating lines can offer higher spatial coherence and therefore higher visibility. A smaller angle of incidence causes a reduction in low-energy x-ray flux due to self-absorption in the jet, but for this application the reduction is negligible. The detector is a scintillator-based fiber-coupled CCD detector from Photonic Science with 5 mg/cm<sup>2</sup> Gadox, a pixel size of  $9 \mu\text{m} \times 9 \mu\text{m}$  and a total area of 36 mm  $\times$  24 mm. Its point spread function (PSF) was measured to have a FWHM of 21  $\mu\text{m}$ .

The arrangements for PBI and GBI are illustrated in Fig. 1(a) and 1(b), respectively. PBI uses the propagation of the wave in free space: the detector is placed some distance away from the sample without any optics. For GBI a Talbot grating interferometer is used, consisting of a phase grating G1 and an absorption grating G2. For our arrangement, G1 has a period  $p_1 = 4.12 \mu\text{m}$ , duty cycle 0.5, and Ni lines of height 10–11  $\mu\text{m}$  on a 50  $\mu\text{m}$  thick Ti substrate. G2 has 60  $\mu\text{m}$  Au lines with a period  $p_2 = 2.4 \mu\text{m}$  and duty cycle 0.5 on a 500  $\mu\text{m}$  thick Si substrate. G1 was mounted on a piezo stage (P-752 from Physik Instrumente) to

enable phase stepping. The experimental arrangement was designed for 25 keV photon energy, and the geometry parameters are shown in Table 1. For GBI the arrangement was chosen taking account of the source spectrum, spot size, and the specifics of available pairs of gratings. For our grating pair, the 3rd fractional Talbot distance is close to the optimal distance by considering the beam coherence length [1]. For PBI the objects were kept at the same distance from the source to keep dose levels the same.

During experiments, objects were immersed in a liquid-paraffin bath to avoid phase-wrapping at the edges. The density of the liquid paraffin is around  $0.8 \text{ g/cm}^3$ . The container was made of 1 mm thick polymethyl methacrylate (PMMA) and was 20 mm thick along the beam propagation direction, adding in total 2 mm of PMMA and up to 18 mm of liquid paraffin. The bath also works as a filter, reducing low energy radiation that increases the dose but cannot reach the detector and contribute to the imaging. Figure 1(c) shows the spectrum after passage through the bath. The strongest peaks around 25 keV are emission lines of In and Sn.

The first object was a phantom made of polyethylene terephthalate (PET) monofilaments of different diameters. The densities of PET is around  $1.4 \text{ g/cm}^3$ . Absorption contrast was significantly reduced due to the similarity of the attenuation coefficients of liquid paraffin and PET. Dark-field images gave little information, as the PET monofilaments have a homogenous structure and smooth surfaces which produce little scattering except at the edges. Therefore for GBI only phase contrast, no absorption-contrast or dark-field images, were considered in the comparison with PBI. The second object was a human breast biopsy sample fixed in formalin in a sample tube with a diameter of 1 cm.

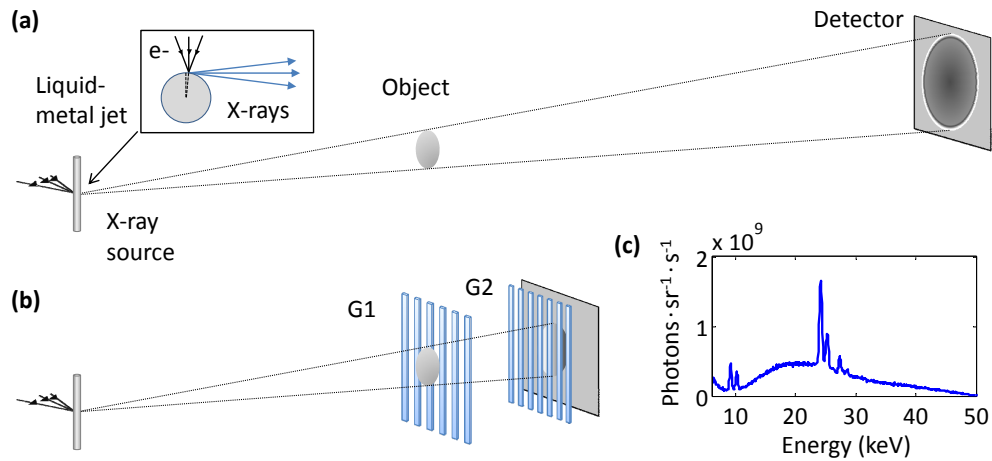


Fig. 1. (a) Experimental arrangement for PBI consisting of the x-ray source, the object and the detector. (b) The same for GBI also including phase (G1) and absorption (G2) gratings. (c) The emission spectrum of the Ga/In/Sn liquid-metal-jet x-ray source after passage through the liquid-paraffin bath.

**Table 1. Geometry parameters of the experiments given as distances from the source**

Distances (m)	Object	G1	G2	Detector
PBI	0.874	-	-	2.188
GBI	0.874	0.903	1.052	1.091

## 2.2 Data processing

For GBI, information about phase, absorption and scattering can be extracted from projections acquired with G2 at different transverse positions with respect to G1 [6]. The detected photon number of one pixel at phase step  $n$  can be modeled in approximation as a sinusoidal curve

$$I(n) = I_0 + a \cos\left(\frac{2\pi n}{N} + \varphi\right), \text{ with } n = 0, 1, \dots, N-1, \quad (1)$$

where  $N$  is the total number of phase-scan steps,  $I_0$  is the mean value of all steps, and  $a$  and  $\varphi$  are amplitude and phase parameters of the sinusoidal curve. These parameters can be evaluated through Fourier series analysis [27]. The  $k$ -th Fourier coefficient  $c(k)$  is

$$c(k) = \frac{1}{N} \sum_{n=0}^{N-1} I(n) \cdot e^{i2\pi \frac{n}{N} k}, \quad (2)$$

which can be obtained using a fast Fourier transform. From this we get the parameters above with the following relations:

$$\begin{aligned} I_0 &= c(0), \\ a &= 2|c(1)|, \\ \varphi &= \arg[c(1)]. \end{aligned} \quad (3)$$

The differential-phase contrast (DPC) image is found as the difference of  $\varphi$  between a scan with the object, and a flat-field scan without it. The DPC signal is proportional to the refraction angle of the wavefront and thus to the first derivative of the phase shift. For PBI projection images, no extra data processing is needed to obtain a phase-contrast image. The edge enhancement is proportional to the second derivative of the phase shift, and subsequent phase retrieval [28] allows reconstruction of the actual phase shift.

The application of a Hilbert filter [29, 30] to the DPC images allowed subsequent tomographic reconstruction. PBI projections were processed using a Fourier-based phase-retrieval algorithm for homogeneous samples by Paganin et al. [31] to reconstruct the projected density. Tomographic reconstructions were performed using cone-beam filtered back projection (FBP) as implemented in the Octopus software [32].

### 2.3 Simulations

Both methods were simulated using Fresnel diffraction theory in a manner similar to Lundström et al. [2] but adding the grating interferometer and scanning process for GBI [14, 26]. The simulation process for the grating-based system is schematically presented in Fig. 2. Firstly, a plane wave is multiplied by the contributions of the object and the first grating, assumed to be in the same plane. The contributions are calculated under the projection approximation [33], using mass attenuation coefficients from NIST [34] and the real part of the complex refractive index from RTAB [35]. A more complex scattering model would allow more accurate simulation of dark-field images, but for the class of the objects considered in this comparison, the dark-field signal is small and not considered in the comparison. Then the field is propagated to the second grating using the Fresnel diffraction integral, evaluated with the fast Fourier transform. The propagation distance is modified to compensate for the spherical wave geometry [31]. After convolution by the projected intensity distribution of the source, the resulting intensity is multiplied by the attenuation function of the second grating. As the field of view is limited by the detector, only the central parts of the gratings are used. Hence the gratings are regarded as thin, and angular filtration due to high aspect ratios omitted. The detector is assumed to be in the same plane as the second grating. The modulation transfer function (MTF) of the detector is measured by the edge method and included in the simulation. The detector quantum efficiency is calculated using the mass energy-absorption coefficients of the phosphor in the Gadox scintillator. The detector response is assumed to be linear with respect to the energy of the detected photons. The full spectrum is represented as a discrete set of energies. Simulations are done for each of these energies, and the resulting intensities are summed for each pixel. Photon noise is considered

and added in accordance to each single projection with the measured noise power spectrum (NPS) and readout noise of the detector. For G2 at different positions with respect to G1, images at different phase scanning steps are obtained. The visibility for GBI

$$V = \frac{a}{I_0} \quad (4)$$

is also affected by imperfections of the gratings, which are difficult to model in the simulation. The difference in visibility between simulation and experiment is corrected for in the simulations by reducing the amplitude in the pixel intensity curves with an experimentally determined constant factor before adding noise.

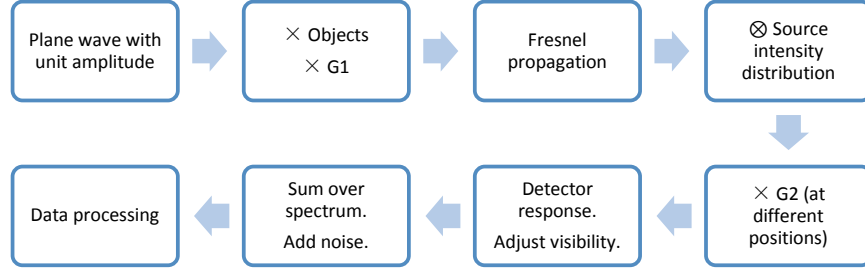


Fig. 2. Schematic illustration of the simulation process for GBI, where  $\times$  indicates multiplication and  $\otimes$  convolution. For PBI, the principle is the same but G1 and G2 are not included.

#### 2.4 Dose and SNR calculation

To keep the time required for simulations at an acceptable level, the absorbed dose was calculated using mass energy-absorption coefficients from NIST [34] taking the shape of the object into account. Comparisons to Monte Carlo simulations performed using the Penelope 2006 software [36] for some PET cylinders and the breast tissue model in liquid paraffin, show that the dose calculated from mass energy-absorption coefficients has, at most, an error of about 23%. In the context of this comparison, which is looking for order-of-magnitude differences, this error is small, and also the same for both methods.

Image quality was assessed through the signal-to-noise ratio in the test statistic of an ideal observer in a detection task. SNR was calculated in Fourier space as [37]

$$\text{SNR}^2 = \iint \frac{|\Delta G(u)|^2}{\text{NPS}(u)} d^2u, \quad (5)$$

where  $\Delta G$  is the difference in the expected signal with and without object and NPS is the noise power spectrum. For PBI and GBI,  $\text{SNR}^2$  was calculated respectively for one projection and for the DPC image, i.e.,  $\Delta G = \Delta\varphi$  for the DPC image. The noise variance,  $\sigma_\varphi^2$ , of the phase signal can be calculated from the noise variance,  $\sigma_n^2$ , of the image at each phase step  $n$  by using the error propagation formula [15, 20, 21]

$$\sigma_\varphi^2 = \frac{2}{V^2 (NI_0)^2} \sum_{n=0}^{N-1} \sigma_n^2. \quad (6)$$

Equation (6) can be simplified to  $\sigma_\varphi^2 = 2/(V^2 NI_0)$  if only photon noise is considered. In a similar manner, error propagation can be used to show that the same relation holds for the covariance. Then it also holds for the NPS, which is a Fourier transform of the covariance. So for the simulations the NPS of the DPC image is found as [22]

$$\text{NPS}_\varphi = \frac{2}{V^2 (NI_0)^2} \sum_{n=0}^{N-1} \text{NPS}_n. \quad (7)$$

### 3. Results and discussions

Figure 3 shows PBI (a-e) and GBI (f-j) images from simulation (a, b, f, g) and experiment (c-e, h-j) of the PET phantom. The experimental DPC images (h) were obtained as the average over 24 DPC images for 5 phase steps with 2 minutes exposure time at each step. The total exposure time was 240 min. The dose was calculated to be around 0.7 Gy for each cylinder, though the value varies slightly for different cylinder diameters. The method for dose simulation was previously verified through measurements using an ionization chamber [2]. To limit drift of the interference fringes during long exposures, the flat-field images were taken in between exposures rather than after as for the propagation-based projections, but the amount was the same for both. The experimental PBI images (c) were averaged over 24 10-minute projections to keep the same dose. The profiles (b, d, g, i) were averaged vertically over the 33 pixels shown in the images for better visualization. For GBI, the reconstructed slice (j) was obtained from a tomographic scan consisting of 360 phase-contrast projections over  $180^\circ$  with  $0.5^\circ$  increment for 5 phase-scanning steps. The exposure time for each phase scanning step is 1 min and consequently 30 h for the whole CT scan, giving a total estimated dose of 5 Gy to each cylinder. The voxel size is  $7.2 \mu\text{m}$ . For PBI, the reconstructed slice (e) was obtained from the same number of phase-retrieved projections with the same total exposure time and consequently the same dose. The voxel size of  $3.6 \mu\text{m}$  differs due to the larger magnification. The visibility of the simulated DPC image was multiplied by 0.44 to match the mean visibility value of the background in the experimental images (15%). As can be seen in Fig. 3, simulations agree with experiments. The small differences that can be seen in the profiles are mainly due to the vertical averaging. As the monofilaments are not perfectly straight and their diameters vary slightly, averaging can easily smear out the high-contrast edge enhancement which only covers a few pixels. Some other factors that can cause differences are uncertainties in the densities of phantom and liquid paraffin, source drift and object instability during long exposures.

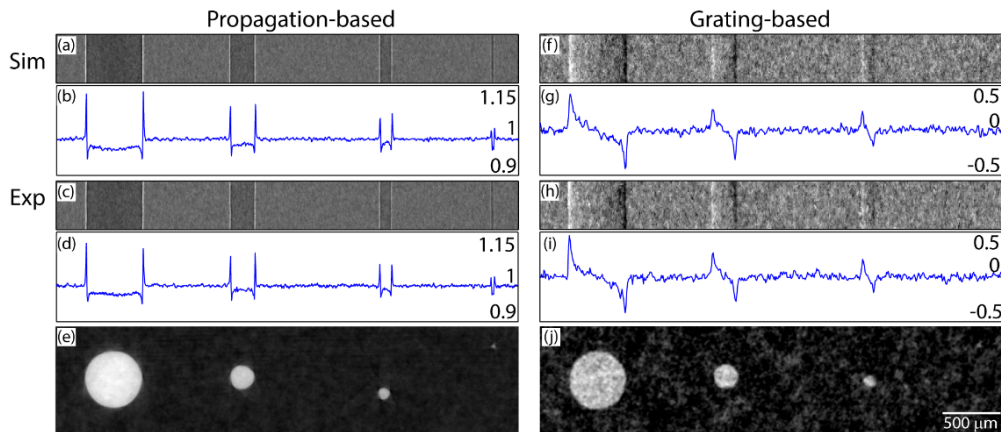


Fig. 3. Simulated and experimental PBI (a-e) and DPC images (f-j) of a phantom consisting of four PET monofilaments in a liquid-paraffin bath. Their diameters were found to be 494, 213, 100 and  $23 \mu\text{m}$  respectively by matching the widths of the simulated images to the experimental ones [38]. Projections (c, h) have 4 h total exposure time. Profiles are integrated vertically over 33 pixels from the images above them. Slices from tomographic reconstructions (e, j) have an exposure time of 30 h.

The simulation in Fig. 4 compares the required dose absorbed in the PET phantom as a function of cylinder diameter for DPC and PBI projection images. The dose was calculated at

the exposure time required to obtain an  $\text{SNR}^2$  of 25, which is a generalization of the Rose criterion for detectability [39]. The  $\text{SNR}^2$  was calculated over a length identical to the cylinder diameter [2] to avoid the effect of cylinder length on the detectability. The DPC and PBI Monochromatic lines were simulated assuming a 25 keV monochromatic source and a flawless grating interferometer optimized for this energy. All other settings were the same as in the experiments. The height of Nickel structure was set to the optimal 8.7  $\mu\text{m}$  instead of the slightly mismatched 10-11  $\mu\text{m}$  used in the experiment for this photon energy. The visibility was 65% for DPC images in this case. For the DPC and PBI Polychromatic lines, a polychromatic source with the spectrum of the liquid-metal-jet source was assumed, giving the DPC images a visibility of 36%. All other settings were kept the same. Unlike PBI, which was not much affected by the wide spectrum, the DPC image has a significant decrease in visibility and increase in dose. Compared to the 25 keV monochromatic source, the low-energy photons lead to a higher dose while contributing less to the DPC signal. The DPC Polychromatic Adjusted line shows the simulation results after adjusting the visibility down to 15% by a factor 0.44 to match the experimental results, where the grating imperfections are assumed to be the main cause. This adjustment increased the required dose roughly 6 times. The PBI Polychromatic Adjusted line is compensated for the mismatch of image contrast between simulations and experiments. The image contrast in experiments is around 18% lower than in simulations. Figure 4 shows that DPC requires higher dose and exposure time to visualize the PET phantoms of the experiments compared to PBI. This result agrees with Fig. 3, where the same dose gives visibly lower noise for the PBI method. The effect is clearest for the finest monofilament of 23  $\mu\text{m}$  diameter, which can be observed in the PBI projection but not in the DPC image with the same exposure time and dose. To resolve the 23  $\mu\text{m}$  phantom would require a dose of around 7 Gy for DPC, but only around 0.09 Gy for PBI projection image. The higher magnification in the PBI setup explains part of its advantage for objects with small diameters.

The dose requirement of PBI has a size dependence of approximately  $d^{-1.9}$ , where  $d$  is the object diameter. The slope of DPC has a size dependence of approximately  $d^{-2.5}$ . The smallest diameters were not considered in the fitting in order to exclude the steeper-slope part in Fig. 4 caused by limited resolution. For PBI, this agrees with earlier results [2], finding a dependence of approximately  $d^{-2}$ . Compared to [19] Diemoz et al., our result supports their conclusion that PBI has higher sensitivity for higher spatial resolution, and also agrees with their experiments that for large-diameter objects (200 and 350  $\mu\text{m}$  wires in [19]) DPC can perform better than PBI projections using a monochromatic source, although differences in both experimental parameters and the methods for calculating SNR led to different specific results. The results also indicate a trend relevant to other microfocus sources, though different source spectrum or spatial coherence properties can give different detailed values for different microfocus sources [10].

The different behavior for different object sizes can be qualitatively explained from the inherent differences of the methods. GBI measures the derivative of the phase, while PBI measures the second derivative. In Fourier space, considering e.g. the contrast transfer function, the first derivative corresponds to a linear dependence on spatial frequency, while the second derivative corresponds to a quadratic dependence. This implies that the methods will depend differently on the spatial frequency and hence on the object size  $d$ , and also that PBI will favor the smaller details more. Hence, while the exact values of the exponents ( $-1.9$  and  $-2.5$ ) might vary with experimental conditions, their approximate values, and the difference between the methods, are likely of more general nature.

The simulations in Fig. 4 were all done using 9  $\mu\text{m}$  pixels, as in this application a high-resolution detector is necessary for high-resolution imaging. For completeness, both methods were simulated using pixel sizes up to  $\sim 50$   $\mu\text{m}$  for monochromatic radiation. Then the required dose of PBI for larger objects increases, as low detector resolution implies the edge

enhancements vital to PBI are not well resolved [19]. The smaller objects are not resolved by either method.

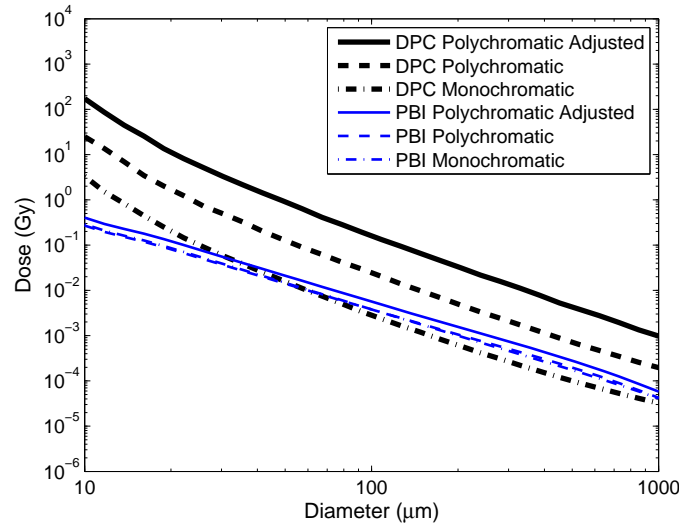


Fig. 4. Simulated dose required for detecting a PET cylinder, in a liquid-paraffin bath, as a function of the cylinder diameter. Simulations for DPC and PBI were done both with a liquid-metal-jet source spectrum and for 25 keV monochromatic x-rays. For the DPC Polychromatic Adjusted line, the visibility was adjusted to agree with the experiments. Similarly, the signal of the PBI Polychromatic Adjusted line was modified to match experimental data.

Figure 5 shows experimental projections and slices of a breast biopsy sample for both PBI and GBI. The main part of the sample is tumor. In Figs. 5(a) and 5(b) adipose tissue can be seen as the brighter area in the left corner and calcifications as small, darker regions in the tumor. The projections for GBI were extracted from an exposure with 2 min exposure time per phase-scanning step and 8 steps, and for PBI an exposure with the same total time, 16 min. A dose of about 54 mGy was estimated to be delivered by simulating the sample as a 1 cm diameter cylinder of breast tissue. The slices were extracted from tomographic scans with 720 projections over 360°. The exposure time per projection is 5 min for both methods (but split into five 1-minute phase steps for GBI). The total dose is estimated to be around 12 Gy. In Fig. 5(b), the absorption contrast is quite high due to the thick object and a significant difference in attenuation coefficient between different materials. Due to the complexity of the biological tissue texture and high noise, it is difficult to distinguish structures using only the phase information in the DPC projection image (c). For the PBI projection (a, d), besides the absorption contrast, the edge enhancement due to phase shift between different tissues offers more information on small details. A tomographic slice of each method is shown in Fig. 5(f)–5(h). The PBI slice (f) was reconstructed from projections, where the phase retrieval parameters were chosen as  $\Delta\beta/\Delta\delta = 0.0079$  to correctly reconstruct the boundary between breast tissue and calcifications. Here,  $\delta$  and  $\beta$  is the real and imaginary part of the refractive index, respectively. The calcifications are assumed to be hydroxyapatite due to their spherical shape [40], as can be seen in Figs. 5(d) and 5(e). The PBI slice (f) seems to have lower noise level than the GBI slices (g) and (h), and adipose tissue and calcifications are more clearly observed. However, in the DPC CT slice (g), the formalin in the tube is also recognizable, which is hard to distinguish in (f) due to the limitation of the assumptions of the phase retrieval.

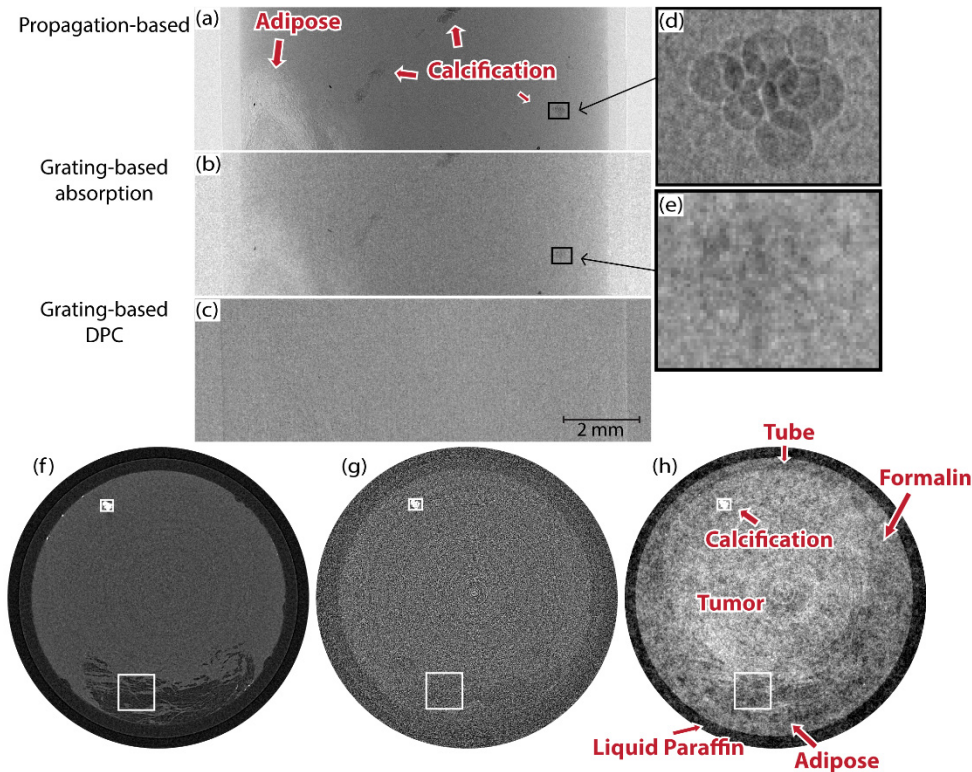


Fig. 5. Projection images of a breast biopsy sample using (a) PBI and (b) GBI absorption and (c) GBI DPC. The exposure time is 16 min per projection for PBI and 2 min times 8 steps for GBI. Inserts (d) and (e) are the enlarged views of a region of  $0.5 \times 0.4 \text{ mm}^2$ , containing calcifications, for PBI and GBI absorption respectively. (a, b, d, e) have a linear color scale from 0.5 to 1.05, where the background is normalized to 1, and (c) from  $-\pi$  to  $\pi$ . Tomography slices using (f) PBI with 5 min exposure time per projection, (g) absorption and (h) DPC from the same data set with 1 min exposure time per phase-scanning step and 5 steps per projection direction. The images were acquired over  $360^\circ$  with  $0.5^\circ$  increment for both methods.

Depending on the region of interest (ROI), different phase-retrieval parameters are needed to correctly reconstruct the interfaces of different materials. Figure 6 shows a magnification of the ROIs marked in Fig. 5. The calcifications (a) and adipose tissue (b) are extracted from Fig. 5(f), using phase-retrieval parameters suitable for viewing the calcifications. Consequently, the calcifications show clearly, but for the adipose tissue there is remaining edge enhancement. The second set of calcifications (c) and adipose tissue (d) are obtained from the same data, but using phase-retrieval parameters suitable for viewing the interface between adipose and breast tissue ( $\Delta\beta/\Delta\delta = 0.0014$ ). Here, the different tissues are well reconstructed, but the calcifications blurred. In comparison, the DPC CT images (e) and (f) give quantitative reconstructions of both calcifications and adipose tissue at the same time. The noise level, however, is higher than for PBI. The GBI absorption images (g) and (h) verify the disadvantage of absorption-contrast imaging on materials such as adipose tissue and breast tissue shown here.

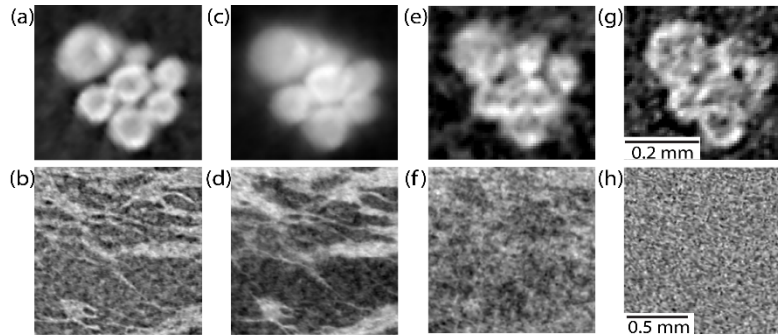


Fig. 6. Magnified images of calcifications (upper row) and adipose tissue (lower row) of PBI reconstructed using parameters of breast tissue and calcifications (a, b) from CT slice Fig. 5(f), PBI reconstructed using parameters of breast tissue and adipose tissue (c, d), GBI DPC (e, f) from CT slice Fig. 5(h), and GBI absorption from slice Fig. 5(g).

#### 4. Conclusion

We have presented a comparison between the PBI and GBI phase-contrast methods based on experiments and simulations for high-resolution laboratory-based imaging. Images of a PET phantom in a liquid-paraffin bath have been acquired for both PBI and GBI systems at the same exposure time and dose. The experiment indicates that PBI projection gives better SNR than GBI DPC at the same exposure time and dose, and also shows a case where PBI projection allows the object to be detected while GBI DPC does not. These results are in agreement with the presented simulations. Doses required for observing objects of different sizes have been calculated and compared for PBI projections and DPC images by simulation. It shows that DPC requires higher doses for all object sizes tested (10-1000  $\mu\text{m}$ ) under the experimental conditions. DPC may have lower dose requirement for large object sizes when a monochromatic source is used. A breast biopsy sample has been imaged and compared using both methods at the same dose, showing the expected improvement in image quality for PBI, but also showing the advantage of quantitative reconstruction of the refractive index, both real and imaginary parts, for GBI.

The specifics of this comparison apply only to the precise arrangements described in this paper, and changing any parameter - source size, distances, grating properties, sample properties, detector properties, to mention some - will influence the results. However, it is possible, partly supported by other comparisons [1, 2, 17, 19], to deduce some more widely applicable trends. For monochromatic radiation and a perfect Talbot interferometer, the method giving the lower dose will depend on object feature size: for small features PBI requires the lower dose, while for larger features GBI requires the lower dose. The exact cut-off point will depend on the circumstances, including e.g. absorption in grating substrates. For polychromatic radiation, as produced by most laboratory sources, PBI requires nearly the same dose as for a monochromatic source, while for GBI dose increases significantly. In addition, grating imperfections can cause significant increase to the dose for GBI. So in some experimental circumstances, such as those presented in this paper, PBI will require the lower dose for a large range of feature sizes.

Finally, we emphasize that the comparison presented in the present paper relates primarily to the required radiation dose and exposure times. Other inherent differences of the methods will sometimes be more relevant, depending on the application. Without any aim for a complete comparison, some of those differences can be mentioned. A main advantage of GBI is its ability to work with multi-material samples without prior knowledge on the compositions of the samples, and the simultaneous acquisition of both phase-contrast, absorption-contrast and dark-field images. Single-distance PBI cannot provide a quantitatively correct reconstruction for multi-material samples. GBI often provides a shorter,

more compact arrangement, relevant to some applications. PBI is mechanically easier to implement, using only a subset of the equipment of grating-based imaging, and more stable from thermal and mechanical point of view. GBI can be used with detectors of larger pixel sizes. PBI does not need a liquid bath and provides easier access to the sample. The dose comparison, as presented in this paper, serves as yet another item on this list, providing more information on which method to use in a dose-sensitive application.

### **Acknowledgments**

We thank Anders Holmberg for his support on phase-stepping mechanics, and Zhentian Wang for the loan of the breast biopsy sample. We acknowledge Karlsruhe Institute of Technology for providing the gratings. Financial support was received from the Swedish Research Council, the Wallenberg Foundation, and the Göran Gustafsson foundation.